 doi 10.1515/ehs-2014-0003 — Energy Harvesting and Systems 2014; 1(1-2): 69–78

Research Article

Armin Feldhoff* and Benjamin Geppert

A High-Temperature Thermoelectric Generator Based on Oxides

Abstract: The thermoelectric energy conversion is described in terms of fluxes of extensive variables entropy and charge, which gives a clear meaning to the figure of merit and to the power factor. Strength and sign of coupling of entropy current and electrical current is decisive for the function of a thermoelectric generator, which was built from n-type and p-type oxide ceramics to be suitable for the high-temperature range. For n-type and p-type legs, $Zn_{0.98}Al_{0.02}O$ and $Ca_3Co_4O_9$-derived ceramics, respectively, were used. Microstructure of both materials was investigated to some detail by X-ray diffraction, scanning electron microscopy, and transmission electron microscopy including elemental analysis. N-type $Zn_{0.98}Al_{0.02}O$ shows sub-micrometre precipitates of $ZnAl_2O_4$ spinel. P-type $Ca_3Co_4O_9$-derived ceramic is a multi-phase composite as the starting powder decomposed partly during sintering. The thermoelectric materials show different temperature slopes of the power factor with the p-type material reaching 1.8 mW cm^{-1} K^{-2} at 1,000 K and the n-type reaching 1.6 mW cm^{-1} K^{-2} at 1,050 K. For the 10-leg thermoelectric generator, a figure of merit of $zT = 0.10$ was estimated at maximum electrical power output when the hot side was at 1,023 K, and a temperature difference of 200 K was applied.

Keywords: high temperature, oxides, entropy conductivity, figure of merit, thermoelectric module

***Corresponding author: Armin Feldhoff,** Institute of Physical Chemistry and Electrochemistry, Leibniz Universität Hannover, Hannover, Lower Saxony, Germany, E-mail: armin.feldhoff@pci.uni-hannover.de
Benjamin Geppert, Institute of Physical Chemistry and Electrochemistry, Leibniz Universität Hannover, Hannover, Lower Saxony, Germany, E-mail: benjamin.geppert@pci.uni-hannover.de

Coupling currents of entropy and charge

When treating the extensive variables entropy S and electrical charge q equal in rank, the description of the thermoelectric effect by the Onsager–de Groot–Callen model (see Callen (2012), Goupil et al. (2011)) takes a highly symmetric form:

$$\begin{pmatrix} \vec{j}_q \\ \vec{j}_S \end{pmatrix} = \begin{pmatrix} \frac{\sigma_T}{q} & \frac{\sigma_T \cdot S^*}{q^2} \\ \frac{\sigma_T \cdot S^*}{q^2} & \frac{\sigma_T \cdot S^{*2}}{q^2} + \Lambda_{\vec{j}_q=0} \end{pmatrix} \cdot \begin{pmatrix} -\vec{\nabla}\eta \\ -\vec{\nabla}T \end{pmatrix} \quad (1)$$

Eq. (1) describes the charge-current density $\vec{j}_q$ and the entropy current density $\vec{j}_S$ which run through a material that is put simultaneously into a gradient of electrochemical potential for the charge carriers $\vec{\nabla}\eta$ and a gradient of the entropy potential $\vec{\nabla}T$, which is the absolute temperature T. It is worth noting that an analogous equation was recently derived by Fuchs (2010) without the need of Onsager's reciprocal relations as a prerequisite. The thermoelectric material acting in this dynamic process is described by the material-specific tensor $\boldsymbol{M}$ with the relevant quantities being explained in the following equation:

$$\boldsymbol{M} = \begin{pmatrix} \frac{\sigma_T}{q} & \frac{\sigma_T \cdot S^*}{q^2} \\ \frac{\sigma_T \cdot S^*}{q^2} & \frac{\sigma_T \cdot S^{*2}}{q^2} + \Lambda_{\vec{j}_q=0} \end{pmatrix} \quad (2)$$

– The charge q, which on the quantum mechanical level of description of the material, is expressed in integer multiples of the elementary charge e, takes the values $q = +e$ if electrons are considered or $q = -e$ if defect electrons are considered; see Ioffe (1960).

- The specific isothermal electrical conductivity σ_T refers to the condition of vanishing gradient in temperature, i.e. $\vec{\nabla} T = 0$.
- The specific entropy conductivity under open-circuit conditions $\Lambda_{\vec{j}_q=0}$, according to Ioffe (1957), is related to the entropy transported by lattice vibrations (phonons as entropy carriers) and electrons as carriers of charge and entropy in case of vanishing electrical current, i.e. $\vec{j}_q = 0$.

  In general, the specific conductivity for thermal energy λ (heat conductivity) depends linearly in temperature T on the entropy conductivity Λ; see Fuchs (2010):

$$\lambda = T \cdot \Lambda \tag{3}$$

- The entropy transport parameter S^* is the ensemble-averaged *entropy per charge carrier* transported through the thermoelectric material; see Zemansky (1957). It is often considered as the decisive parameter in the coupling of entropy current and charge current as in the case of $S^* = 0$ the material's tensor simplifies in loosing the coupling non-diagonal elements and the charge-current coupled entropy conductivity (see also eq. 9):

$$\boldsymbol{M}' = \begin{pmatrix} \frac{\sigma_T}{q} & 0 \\ 0 & \Lambda_{\vec{j}_q=0} \end{pmatrix} \tag{4}$$

  However, for an absolute electrical isolator with $\sigma_T = 0$, the material's tensor (eq. 2) will have an even more rudimentary form.

  Remember, instead of the entropy per charge carrier S^*, widely the Seebeck coefficient α is used to describe the material's property, which has then the meaning of entropy transported per unit charge; see Scott (1962), Goupil et al. (2011):

$$\alpha = \frac{S^*}{q} \tag{5}$$

  It is important to note that charge and entropy currents can couple in the same direction or in counterdirection with each other. This is reflected in the sign of α which can be positive or negative for a specific material; see Ioffe (1957). Among semiconducting materials the situation is such that α(n-type)<0 and α(p-type) > 0, and for a thermoelectric energy harvesting device it is decisive to have both signs of α available (see Figure 1).

If the local electrochemical potential of the charge carriers $\eta(\vec{x})$ and the local entropy potential, i.e. the absolute temperature $T(\vec{x})$, are taken into consideration, the power density p, i.e. energy current density $\vec{j}_E$, flowing through the material $\boldsymbol{M}$, can be derived from eq. (1):

$$\begin{aligned} p = |\vec{j}_E| &= |(\eta(\vec{x}), \quad T(\vec{x}))\cdot \begin{pmatrix} \vec{j}_q \\ \vec{j}_S \end{pmatrix}| \\ &= |\eta(\vec{x})\cdot\vec{j}_q + T(\vec{x})\cdot\vec{j}_S| \\ &= |\vec{j}_{E,\,\text{electrical}}(\vec{x}) + \vec{j}_{E,\,\text{thermal}}(\vec{x})| \end{aligned} \tag{6}$$

Eq. (6) describes energy conversion function of material $\boldsymbol{M}$ by the total power density p being the absolute value of the sum of the electrical power density $\eta\cdot\vec{j}_q$ and the thermal power density $T\cdot\vec{j}_S$, which locally vary while p being constant under steady-state conditions.

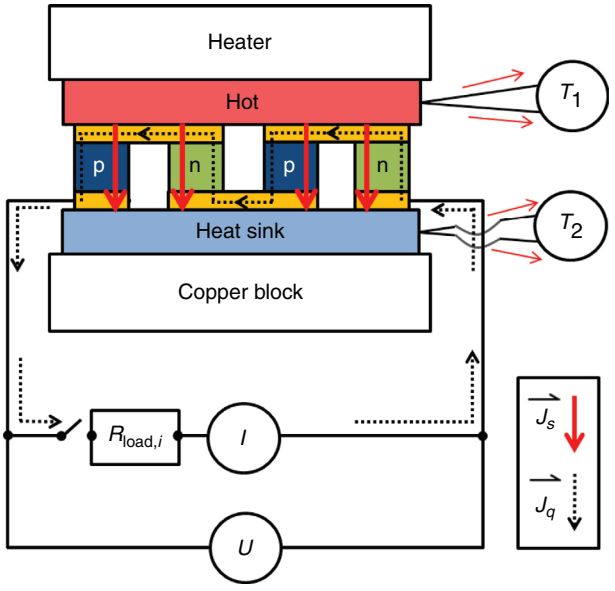

Figure 1 Scheme of the measurement setup for characterisation of the thermoelectric oxide-based generator. Note the alternating coupling directions of entropy current $\vec{j}_S$ and electrical current $\vec{j}_q$ in p-type ($\alpha > 0$) and n-type (α<0) legs. In case of electrical closed-circuit, a circular electrical current (drawn in dotted lines) is driven by entropy currents, which expresses the energy conversion described by eq. (6). The Pt–Rh thermocouples for measuring temperatures T_1 and T_2 constitute thermoelectric devices operating in electrical open-circuit conditions. Here, entropy fluxes are essential but small as compared to the ones running the generator

Materials' challenge

In the context of thermoelectric energy harvesting, materials are of advantage which provide high efficiency in the energy conversion process described by eq. (6). Now let us have a look on tensor element M_{22} in eq. (2), which

describes the entropy conductivity Λ_η at constant electrochemical potential (short circuit). Let us postulate that high efficiency can be achieved if the ratio of the entropy conductivity under short-circuit conditions Λ_η and the entropy current density under open-circuit conditions $\Lambda_{\boldsymbol{j}_q=0}$ is large:

$$\begin{aligned}\frac{\Lambda_\eta}{\Lambda_{\boldsymbol{j}_q=0}} &= \frac{\frac{\sigma_T \cdot S^{*2}}{q^2} + \Lambda_{\boldsymbol{j}_q=0}}{\Lambda_{\boldsymbol{j}_q=0}} = \frac{\sigma_T \cdot \alpha^2 + \Lambda_{\boldsymbol{j}_q=0}}{\Lambda_{\boldsymbol{j}_q=0}} \\ &= \frac{\sigma_T \cdot \alpha^2}{\Lambda_{\boldsymbol{j}_q=0}} + 1 := zT + 1\end{aligned} \tag{7}$$

The parameter zT denotes the figure of merit of the thermoelectric material, and it was originally derived by Ioffe (1957) by thermodynamic analysis of a thermoelectric device. The higher the figure of merit zT, the better the material:

$$zT := \frac{\sigma_T \cdot \alpha^2}{\Lambda_{\vec{\boldsymbol{j}}_q=0}} \tag{8}$$

It is obvious that the figure of merit zT only depends on three parameters of materials and a temperature dependence is given inherently by $\sigma_T = \sigma_T(T)$, $\alpha = \alpha(T)$, and $\Lambda = \Lambda(T)$. It is worth noting that all these three parameters are tensors by principle but for ease of discussion are treated as scalars (i.e. trace of tensor) throughout the manuscript. The approach of treating entropy and entropy conductivity equal in rank to charge and electrical conductivity, respectively, gives a clearer understanding of the figure of merit than the traditional treatment; see Goupil et al. (2011).

While the estimation of the figure of merit zT in the high-temperature range involves measurement of thermal conductivity Λ with expensive equipment, we followed the straightforward approach to choose materials on the basis of the so-called power factor and estimate their functional properties in an integrative manner when built into a thermoelectric module using principle described by Min and Rowe (2001). The power factor $\sigma_T \cdot \alpha^2$ has the meaning of a charge-current coupled specific entropy conductivity and constitutes one of the two summands in the material's tensor element $M_{22} = \Lambda_\eta$:

$$\Lambda_{\vec{\boldsymbol{j}}_q\text{-coupled}} = \Lambda_\eta - \Lambda_{\vec{\boldsymbol{j}}_q=0} = \frac{\sigma_T \cdot S^{*2}}{q^2} = \sigma_T \cdot \alpha^2 \tag{9}$$

In low-temperature applications, non-oxide thermoelectric materials are established. By nanostructuring telluride systems, impressive maximum values of the figure of merit were demonstrated; see Poudel et al. (2008), Biswas et al. (2011). However, under high-temperature conditions the figure of merit is poor, and moreover, the electronic structure of these semiconducting materials is easily degraded by oxidation. It is that BiTe-systems are thermally stable to about 500 K and PbTe-systems up to 700 K; see Minnich et al. (2009). To operate thermoelectric energy harvester reliably at higher temperatures, which is of interest for example in the automotive exhaust system with temperatures in the range of 1,000–1,200 K, see Rowe et al. (2011), alternative materials have to be considered. If stability at high temperature comes into account, oxide ceramics are the materials of choice and quite some stoichiometries and crystal structures have been investigated so far; see Koumoto et al. (2013), Ohtaki (2011), Wunderlich (2013). Among the oxides, n-type $Zn_{0.98}Al_{0.02}O$ and p-type $Ca_3Co_4O_9$ constitute the most promising compositions, and they were used in our study to construct a thermoelectric harvester for the high-temperature range; see Vogel-Schäuble et al. (2011).

Experimental

Powders of n-type $Zn_{0.98}Al_{0.02}O$ and p-type $Ca_3Co_4O_9$ thermoelectric materials were synthesised by a sol–gel route as described by Feldhoff et al. (2008). The nitrates of respective metal cations were stoichiometrically added to an aqueous ammonia solution of pH = 9 containing citric acid and ethylenediaminetetraacetic acid (EDTA) for complexing the dissolved metal ions. The obtained precipitates were calcinated at 950 K for 10 h with a heating and cooling rate of 3 min K^{-1}. The calcinated powder products were cold-pressed and sintered. The n-type $Zn_{0.98}Al_{0.02}O$ was sintered at 1,673 K for 10 h with a heating and cooling rate of 2 min K^{-1}, while p-type $Ca_3Co_4O_9$ was sintered at 1,423 K for 10 h with the same heating and cooling parameters. For $Ca_3Co_4O_9$, sintering parameters were thus chosen to obtain a dense ceramic on the cost of partial decomposition of the compound; see Moon et al. (2001).

Phase composition of the obtained bulk materials for n-type and p-type semiconduction was analysed by X-ray diffraction (XRD) using a Bruker D8 Advance with Cu-K_α radiation. Materials' microstructure was investigated by a field-emission scanning electron microscope of the type JEOL JSM-6700F which was equipped with an energy-dispersive X-ray spectrometer (EDXS) of the type Oxford Instruments INCA 300 for elemental analysis. Specimen for SEM were vibration-polished on a Buehler VibroMet 2 using 50 nm colloidal alumina suspension. The p-type material was investigated further by a 200 kV field-emission transmission electron microscope of the type JEOL

JEM-2100F. The TEM was operated in different modes: scanning TEM (STEM), EDXS, selected area electron diffraction (SAED), and high-resolution TEM (HRTEM). For further elemental analysis with electron-energy-loss spectroscopy, a Gatan Imaging Filter (GIF 2100) was employed. Specimen for TEM was prepared by polishing to 20 μm thickness on diamond-lapping films (Allied High Tech Multiprep) and final thinning by 3 kV argon ion beam (Gatan PIPS).

For thermoelectric characterisation of the materials, electrical conductivity and Seebeck coefficient were measured depending on the temperature. From these parameters, the power factor $\sigma_T \cdot \alpha^2$ was estimated for each compound. Thermoelectric properties were measured on a home-made measurement cell, which was installed on a vertical single-zone split-furnace (Elite Thermal Systems Ltd). The electronic parameters were measured with Keithley 2100 $6\frac{1}{2}$ digit multimeters and converted with Lab View software.

To characterise the thermoelectric module and estimate zT for the generator, load-resistance-dependent measurements under steady-state conditions were made. The measurement setup is shown in Figure 1.

Materials' microstructure and power factor

To get a view inside the materials by SEM, the sintered oxide ceramics were prepared by vibration polishing. Figure 2 shows the results of structural investigations for n-type $Zn_{0.98}Al_{0.02}O$ and p-type $Ca_3Co_4O_9$-derived ceramics.

The SEM micrograph of vibration-polished $Zn_{0.98}Al_{0.02}O$ shows grain sizes of the n-type material in the range from 10 μm to 40 μm. Aluminium-rich particles are distributed inside the material, which were identified as $ZnAl_2O_4$ phase by spinel-type reflections in XRD analyses. These precipitates have grain sizes from about 200 nm to 5 μm. The p-type $Ca_3Co_4O_9$-derived material has a porous structure. The pores are isolated and do not form a connected network. After vibration polishing, the pores were partly filled with Al_2O_3 nanoparticles from the polishing suspension which are noticed as Al signal in the EDXS analysis. Some Co-rich phase is distributed inside the material. No contrast between individual grains could be made visible by using SEM on vibration-polished cross-section. The sintered material shows poor

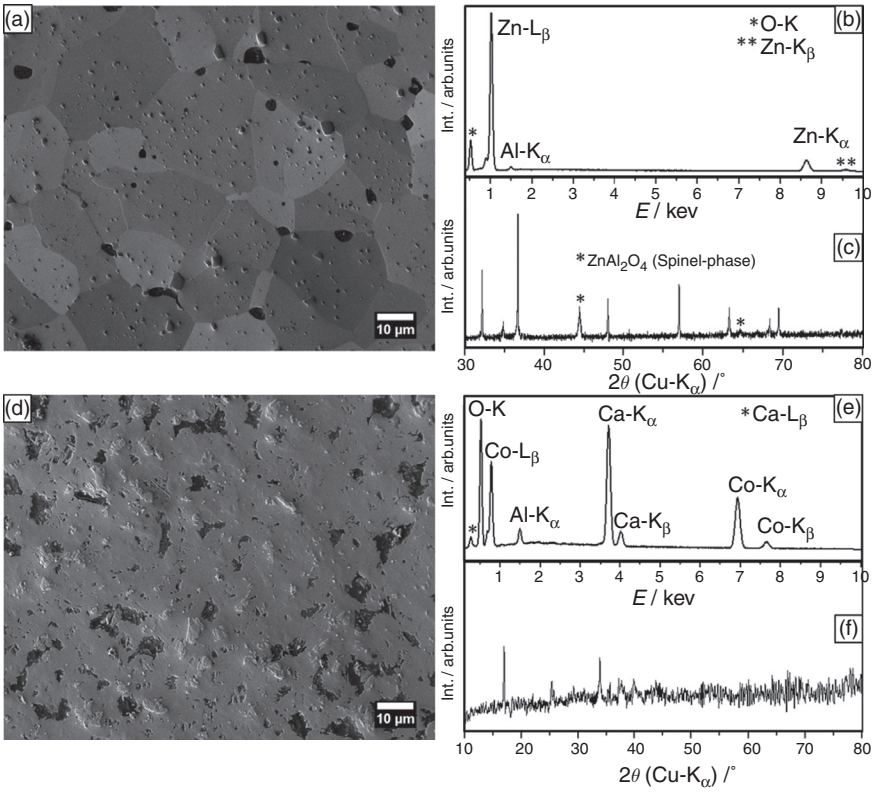

Figure 2 Sintered ceramics analysed by vibration-polished cross-section in SEM, EDX spectra, and XRD pattern: (a–c) $Zn_{0.98}Al_{0.02}O$ and (d–f) $Ca_3Co_4O_9$-derived

Note: Black contrast refers to internal porosity.

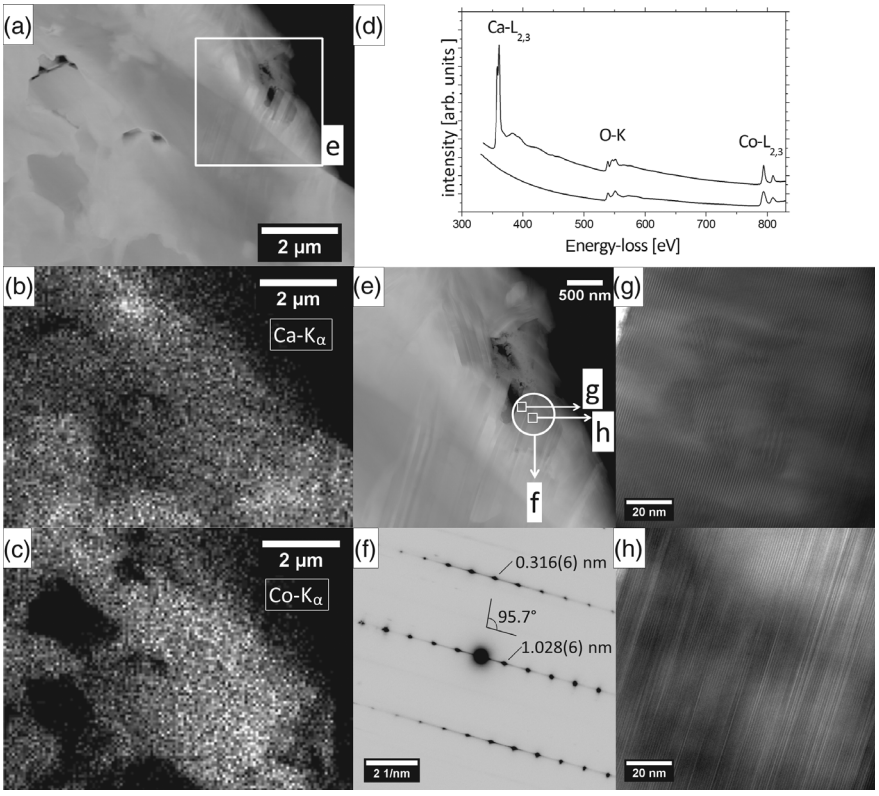

Figure 3 TEM analysis of the $Ca_3Co_4O_9$-derived ceramic: (a) STEM annular dark-field micrograph, (b) EDXS elemental map of calcium, (c) EDXS elemental map of cobalt, (d) EEL spectra of calcium-cobalt oxide and of cobalt oxide as local phases, (e) higher magnification STEM annular dark-field micrograph, (f) electron diffraction pattern from the 560 nm circular area indicated in (e), and (g, h) HRTEM micrographs of areas indicated in (e)

crystallinity in XRD. The diffraction data in Figure 2(f) show broadened reflections on the Ca–Co–O structure in the 2Θ range from 15° to 50° at low intensity, which is noticed on large background noise.

For detailed structure analyses, TEM investigations were made from p-type $Ca_3Co_4O_9$-derived ceramic and surprisingly showed well-developed crystallinity. Figure 3(a) shows grains in the size of up to 2 µm. The EDXS elemental distribution of calcium and cobalt in Figure 3(b) varies locally. EEL spectra investigations in Figure 3(b) show exemplarily ionisation edges of a complex calcium-cobalt oxide and cobalt oxide, which are present as local phases. A detailed area in the higher magnification micrograph of Figure 3(e) was investigated further. The SAED pattern shows a large lattice plane distance of 1.028 nm which is in the typical range of misfit-layered cobaltites as $Ca_3Co_4O_9$ (see Masset et al. (2000), PDF no. 00-058-0661) or $Ca_3Co_2O_6$ (see Fjellvåg et al. (1996), ICSD no. 160557). However, the zone axis pattern could not be indexed according to the known phases in powder-diffraction files (PDF) or inorganic crystal structure database (ICSD) entries. In the decomposition during sintering at 1,423 K, probably phases are formed, which were not reported before. Anyway, the high-resolution micrographs from close-by regions in Figure 3(e) vary from a widely regular structure with some nanoprecipitates in Figure 3(g) to a structure with high density of stacking faults in Figure 3(h). The aforementioned poor X-ray crystallinity is probably the consequence of phase separation resulting in a multi-phase material with misfitted systems consisting of different local amounts of Ca and Co in the oxide matrix. There are several stoichiometric phases referring to the Ca–Co–O system; see Koumoto, Terasaki, and Funahashi (2006), Miyazaki et al. (2000, 2002). Based on the TEM investigations, the p-type ceramic can be considered as a multi-component composite material, which has conserved some misfit-layered cobaltite.

For both materials, electrical conductivity σ_T and the Seebeck coefficient α (from thermovoltage) were measured as function of temperature. These data allowed to obtain the power factor according to eq. (9). The

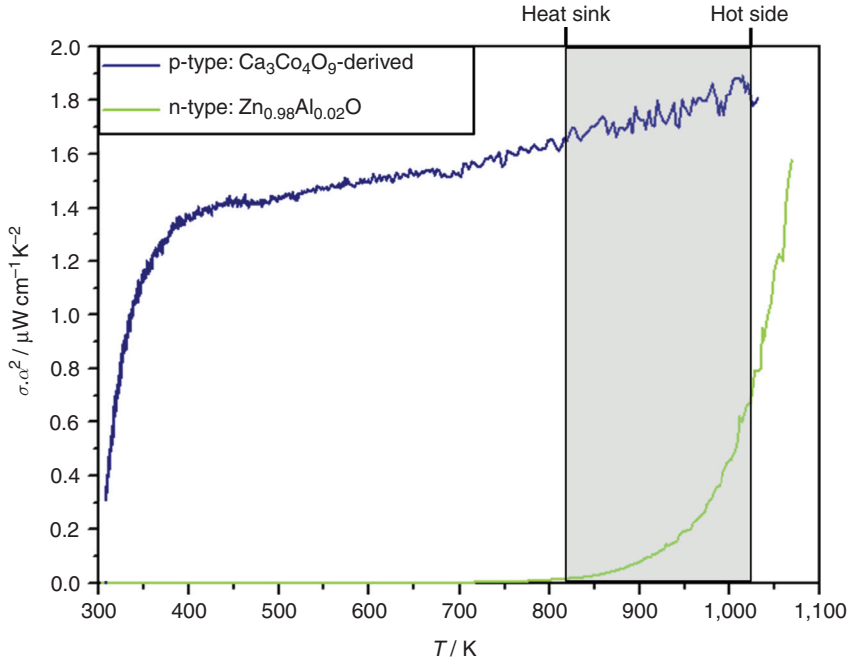

Figure 4 Power factors of n-type $Zn_{0.98}Al_{0.02}O$ and p-type $Ca_3Co_4O_9$-derived materials show different degrees of temperature dependence. The temperature interval used for investigation of the thermoelectric generator is marked

temperature dependence of the power factor for both materials is shown in Figure 4.

With increasing temperature, the power factor of the p-type material increases rapidly and reaches a value of 1.4 mW cm^{-1} K^{-2} at 400 K. Continuing from 400 K, the power factor increases slower and reaches a value of 1.8 mW cm^{-1} K^{-2} at 1,000 K. The power factor of the n-type material is limited by the electrical conductivity. At 800 K the power factor starts to increase exponentially and reaches a value of 1.6 mW cm^{-1} K^{-2} at 1,050 K. In the relevant temperature interval between 823 K and 1,023 K, the power factor of the n-type material, however, does not reach that of the p-type material.

Thermoelectric generator

The obtained disc-shaped ceramic bulk materials were cut by a wire saw to produce the semiconducting legs for constructing a thermoelectric oxide-based generator. The module was constructed by contacting five n-type and five p-type semiconductor legs in electrical serial connection using a gold-paste from HERAEUS. The electrical isolating cover-plates were made of Al_2O_3. Wires consisting of Pt were attached to connect the external electrical circuit. The prepared module was baked in a furnace at 1,223 K for 2 h to harden the gold-paste to obtain a mechanical stable device with contacts of metallic gold. The connected ends of each of the 3 mm long semiconducting legs have an area of 1.5 mm^2 per leg. A scheme and a side-view photograph of the constructed generator are shown in Figure 5.

The hot side of the device was heated up to 1,023 K, while a temperature gradient was established to have a temperature drop of $\Delta T = 200$ K. After an equilibration time of 1 h, different load resistances $R_{\mathrm{load},i}$ $(i = 1 - 6)$ were switched into the external electrical circuit. The electronic parameters I (electrical current) and U (voltage) were measured. The electrical power density ρ_{el} was calculated from received data P_{el} (electrical power output) and effective area. The mentioned parameters are shown in Figure 6 which depend on the switched load resistance.

Every interval last about 3 min. The first interval with closed-circuit conditions was measured without any external load resistance; i.e. $R_{\mathrm{load},1} = 0$. The electrical power output P_{el} refers to the module, while the electrical power density is the ratio of P_{el} and the effective cross-area of thermoelectric legs, which is 0.15 cm^2 when summarising over all 10 legs. In Figure 7, the measured data points are fitted to continuous plots of U and P_{el} versus I.

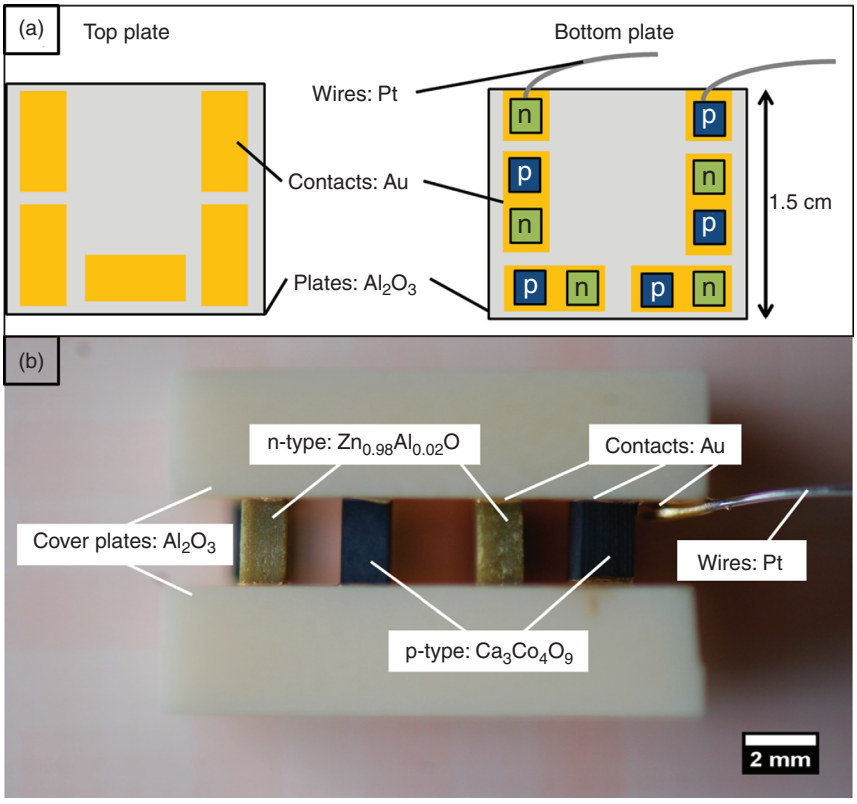

Figure 5 Constructed thermoelectric oxide-based generator: (a) scheme of the inner view of the generator and (b) side-view photograph of the generator

From the fitted data in Figure 7, the maximum electrical output power P_{max} and the respective electrical current $I(P_{max})$ were estimated while the voltage $U(P_{max})$ can be read from the linear fit.

The open-circuit voltage U_{OC} can also be determined from Figures 6 and 7. The calculated parameters at presented thermal steady-state conditions are given in Table 1.

The electrical output power P_{el} depending on various load resistances R_{load} can be expressed by eq. (10), which follows from Figure 7 by geometrical considerations.

$$P_{el} = \frac{U_{OC}^2}{4 \cdot R_{load} \cdot \frac{U_{OC} - U_{load}}{U_{load}}} \tag{10}$$

At the load-dependent maximum output power P_{max}, there is $R_{load} = R_{module}$ and eq. (10) becomes

$$P_{max} = \frac{U_{OC}^2}{4 \cdot R_{module}} \tag{11}$$

With the relationship seen in eq. (10), the electrical resistance of the thermoelectric module at 1,023 K was calculated. With the principle described by Min and Rowe (2001), zT was calculated using the obtained electrical parameter values at thermal steady-state conditions. The finally used relationship is given in eq. (12)

$$zT = \frac{U_{OC}}{I(P_{max}) \cdot R_{module}} - 1 \tag{12}$$

The figure of merit for the module, according to eqs (8) and (9), states the ratio of charge-current coupled entropy conductivity and open-circuit entropy conductivity, was thus estimated in a direct manner by electrical measurements alone. The result is given in Table 1 together with other relevant thermoelectric parameters.

Conclusions

The n-type $Zn_{0.98}Al_{0.02}O$ and p-type $Ca_3Co_4O_9$-derived materials are suitable for constructing an oxide-based thermoelectric generator for high-temperature application. The low-cost materials show good thermal and electrical stability. There were also no problems referring to

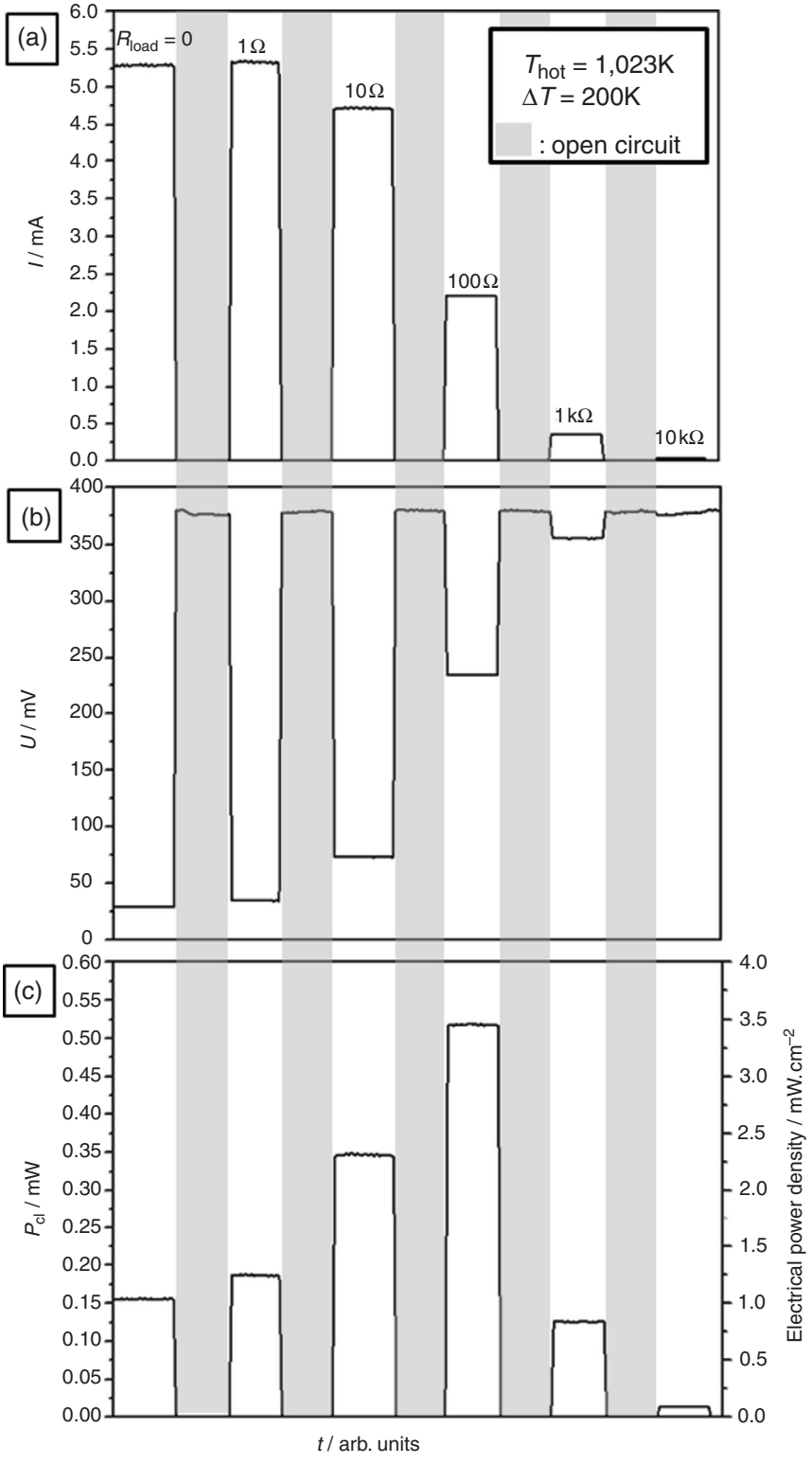

Figure 6 Thermoelectric performance depending on the integrated load resistance $R_{\mathrm{load},i}$ at thermal steady-state conditions. The index i refers to switching between different resistances from $R_{\mathrm{load},1} = 0$ to $R_{\mathrm{load},6} = 10\mathrm{k}\Omega$

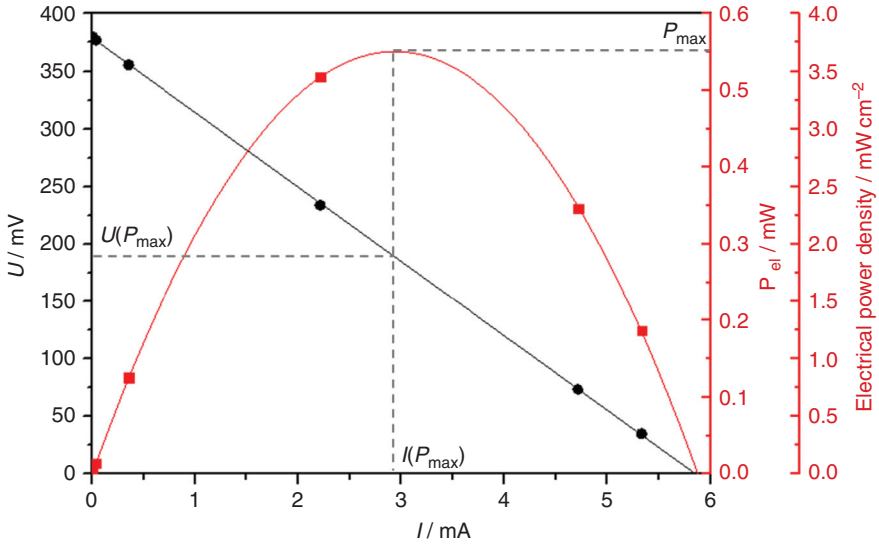

Figure 7 Module characteristics at 1,023 K/823 K from fitting time-averaged values shown in Figure 6. Labelled values of $U(P_{max})$ and $I(P_{max})$ at maximum electrical output power were used for estimating the figure of merit

Table 1 Determined thermoelectrical parameters of the oxide-based generator at maximum electrical power output P_{max} under 1,023 K/823 K conditions

T_{hot}/K	$\Delta T/K$	$R_{module} = R_{load}/\Omega$	P_{max}/mW	$I(P_{max})/mA$	$U(P_{max})/mV$	U_{OC}/mV	I_{SC}/mA	zT
1,023	200	65.40	0.55	2.94	189	379	5.79	0.10

thermal expansion mismatch of synthesised oxides. At maximum electrical output power, the module reached a figure of merit of $zT = 0.10$ at a hot-junction temperature of 1,023 K and a temperature difference of 200 K. Potential to improve the generator over these achievements is given in the microstructure of the materials. The p-type $Ca_3Co_4O_9$-derived ceramic turned out to be a multi-component composite. Optimised sintering parameters will preserve a higher amount of misfit-layered cobaltite starting phase in the final ceramic product. Higher impact, however, can be expected by improvements of the n-type $Zn_{0.98}Al_{0.02}O$, which, in the temperature range of interest, showed a distinctly smaller power factor than the p-type material. The electronic conductivity limits the power factor of n-type $Zn_{0.98}Al_{0.02}O$. Doping the material to increase the charge carrier concentration should be done. With increasing electrical conductivity of the n-type material, the resistance of the module will be decreased. This can effect a greater electrical current coupling with the entropy current. Furthermore, the dependence of the count of integrated legs on the electric parameters should be investigated.

References

Biswas, K., J. He, I. Blum, C.-I. Wu, T. Hogan, D. Seidman, V. Dravid, and M. Kanatzidis. 2011. "High-Performance Bulk Thermoelectrics with All-Scale Hierarchical Architectures." *Nature* 119:770–75.

Callen, H. 2012. "The Application of Onsager's Reciprocal Relations to Thermoelectric, Thermomagnetic, and Galvanomagnetic Effects." *Physical Review* 489:414–18.

Feldhoff, A., M. Arnold, J. Martynczuk, T. Gesing, and H. Wang. 2008. "The Sol-Gel Synthesis of Perovskites by EDTA/Citrate Complexing Method Involves Nanoscale Solid State Reactions." *Solid State Science* 10:689–701.

Fjellvåg, H., E. Gulbrandsen, S. Assland, A. Olsen, and B. Hauback. 1996. "Crystal Structure and Possible Charge Ordering in

One-Dimensional $Ca_3Co_2O_6$." *Journal of Solid State Chemistry* 124:190–94.

Fuchs, H. 2010. *The Dynamics of Heat – A Unified Approach to Thermodynamics and Heat Transfer*, 2nd ed. Graduate Texts in Physics. New York: Springer.

Goupil, C., W. Seifert, K. Zabrocki, E. Müller, and G. Snyder. 2011. "Thermodynamics of Thermoelectric Phenomena and Applications." *Entropy* 13:1381–517.

Ioffe, A. 1957. *Semiconductor Thermoelements and Thermoelectric Cooling*, 1st ed. London: Infosearch.

Ioffe, A. 1960. *Physics of Semiconductors*, 1st ed. London: Infosearch.

Koumoto, K., R. Funahashi, E. Guilmeau, Y. Miyazaki, A. Weidenkaff, Y. Wang, and C. Wan. 2013. "Thermoelectric Ceramics for Energy Harvesting." *Journal of the American Ceramic Society* 96:1–23.

Koumoto, K., I. Terasaki, and R. Funahashi. 2006. "Complex Oxide Materials for Potential Thermoelectric Applications." *MRS Bulletin* 31:206–10.

Masset, A., C. Michel, A. Maignan, M. Hervieu, O. Toulemonde, F. Studer, B. Raveau, and J. Heitjmanek. 2000. "Misfit-Layered Cobaltite with an Anisotropic Giant Magnetoresistance: $Ca_3Co_4O_9$." *Journal of Physical Review B* 62:166–75.

Min, G., and D. Rowe. 2001. "A Novel Principle Allowing Rapid and Accurate Measurement of a Dimensionless Thermoelectric Figure of Merit." *Measurement Science and Technology* 12:1261–62.

Minnich, A., M. Dresselhaus, Z. Ren, and G. Chen. 2009. "Bulk Nanostructured Materials: Current Research and Future Prospects." *Energy and Environmental Science* 2:466–79.

Miyazaki, Y., K. Kudo, M. Akoshima, Y. Ono, Y. Koike, and T. Kajitani. 2000. "Modulated Structure of Thermoelectric Compound $[Ca_2CoO_3]CoO_2$." *Journal of the Physical Society of Japan* 39: L531–L533.

Miyazaki, Y., M. Onoda, T. Oku, M. Kikuchi, Y. Ishii, Y. Ono, Y. Morii, and T. Kajitani. 2002. "Modulated Structure of Thermoelectric Compound $[Ca_2CoO_3]CoO_2$." *Journal of the Physical Society of Japan* 71:491–97.

Moon, J., D. Nagahama, Y. Masuda, W. Seo, and K. Kouomoto. 2001. "Anisotropic Thermoelectric Properties of Crystal-Axis Oriented Ceramics of Layer-Structured Oxide in the Ca-Co-O System." *Journal of the Ceramic Society of Japan* 109:647–50.

Ohtaki, M. 2011. "Recent Aspects of Oxide Thermoelectric Materials for Power Generation from Mid-to-High Temperature Heat Source." *Journal of the Ceramic Society of Japan* 119:770–75.

Poudel, B., Q. Hao, Y. Ma, Y. Lan, A. Minnich, B. Yu, X. Yan, D. Wang, A. Muto, D. Vashaee, et al. 2008. "High-Thermoelectric Performance of Nanostructured Bismuth Antimony Telluride Bulk Alloys." *Science* 320:634–38.

Rowe, D., J. Smith, G. Thomas, and G. Min. 2011. "Weight Penalty Incurred in Thermoelectric Recovery of Automobile Exhaust Heat." *Journal of Electronic Materials* 40:784–88.

Scott, W. 1962. "Electron Levels, Electrochemical Effects, and Thermoelectricity." *American Journal of Physics* 30:727–37.

Vogel-Schäuble, N., R. Dujardin, A. Weidenkaff, and M. Aguirre. 2011. "Influence of Thermal Aging Phenomena on Thermoelectric Properties of Al-Substituted ZnO." *Journal of Electronic Materials* 41:1606–14.

Wunderlich, W. 2013. "Large Seebeck Voltage of Co, Mn, Ni, Fe-Ceramics." *Advances in Ceramic Science and Engineering* 2:9–15.

Zemansky, M. 1957. *Heat and Thermodynamics*, 4th ed. New York: McGraw Hill.